

Tabletop deep-ultraviolet transient grating for ultrafast nanoscale carrier-transport measurements in ultrawide-band-gap materials

Emma E. Nelson^{1,*}, Brendan McBennett¹, Theodore H. Culman¹, Albert Beardo¹, Henry C. Kapteyn^{1,2}, Matthew H. Frey³, Matthew R. Atkinson³, Margaret M. Murnane¹, and Joshua L. Knobloch¹

¹Department of Physics, JILA, and STROBE NSF Science and Technology Center, University of Colorado and NIST, Boulder, Colorado 80309, USA

²KMLabs Inc., 4775 Walnut St. #102, Boulder, Colorado 80309, USA

³3M Corporate Research Laboratory, 3M Center, St. Paul, Minnesota 55144, USA



(Received 3 July 2024; revised 22 August 2024; accepted 25 September 2024; published 4 November 2024)

Understanding nanoscale electron and phonon transport is critical for the development of next-generation semiconductor technologies, where deviations from macroscopic behaviors can either limit or enhance device performance. While transient gratings generated by the interference of visible lasers can directly excite microscopic, nonequilibrium charge and heat distributions in metals and traditional semiconductors, extending this noncontact approach to ultrawide-bandgap materials involves added complexities. To address these challenges, here we introduce a tabletop deep-ultraviolet (DUV; 6.3 eV) transient grating setup, and show that it supports sub-300 nm spatial and subpicosecond temporal resolution. As an initial demonstration, we excite and probe gigahertz surface acoustic waves in thin gold films. We then perform DUV transient grating measurements of nanoscale carrier transport in diamond and discuss the carrier concentration-dependent diffusion coefficient. This DUV transient grating capability provides a versatile, noncontact tool for investigating transport at length scales below the visible diffraction limit and in wide-bandgap materials, and bridges the gap between visible and facility-scale extreme-ultraviolet transient grating capabilities.

DOI: 10.1103/PhysRevApplied.22.054007

I. INTRODUCTION

Characterization of dynamic physical processes critical for a host of technologies has long been a key application of pulsed laser light. Laser-based characterization techniques are frequently used as nondestructive, non-contact probes of the optical, electrical, mechanical, thermal, magnetic, structural, and chemical properties of materials. In particular, the transient grating (TG) technique is a powerful and versatile laser-based characterization tool that, over the past half-century, has investigated thermophysical properties [1–3], charge transport [4,5], spin dynamics [6], interfacial properties [7], residual stress [8], structural [9], acoustic waves [10,11], and a host of other dynamical behaviors [12–14] in a variety of materials including metals, semiconductors, dielectrics, and polymers in addition to the physical properties of liquids [15,16] and the chemical composition and temperature of gases [17]. The TG technique consists of two excitation “pump” laser pulses that interfere to create a microscopic sinusoidal excitation pattern in a sample, generating nonequilibrium conditions

that relax through various dynamical processes [14,18,19]. Then, by monitoring diffracted light from a time-delayed “probe” beam, the dynamic relaxation to equilibrium can be tracked in order to extract physical properties or understand fundamental transport mechanisms.

Traditional TG experiments utilize infrared or visible laser light, due to the prevalence of commercial lasers at these wavelengths. Such visible-based TG experiments can access nanoscale electron and phonon transport in relatively small bandgap semiconductors, including two-dimensional (2D) materials such as MoS₂, with pump spatial periods above 500 nm [20,21]. However, this limits the materials that can be studied and the accessible length scales. Future power electronics and high-frequency communication and computational devices rely on the integration of both 2D and 3D wide- and ultrawide-bandgap materials, such as diamond or nitrides, rather than silicon, due to their favorable material properties including high electric field breakdown strength [22,23]. The limited understanding of nonequilibrium charge and heat transport processes in these materials, especially at the length scales present in current electronic devices, represents a key barrier to their use in applications; for example, the

*Contact author: emne4121@colorado.edu

unpredictable emergence of hot spots and residual heat and charge losses dramatically affects device performance and lifetime. Therefore, the ability to measure and predict the electronic, thermal, and mechanical performance of ultrawide-bandgap semiconductors by direct excitation is crucial for envisioning next-generation devices [23,24]. In pioneering work, Malinauskas *et al.* harnessed deep-ultraviolet (DUV) light in a TG geometry to measure carrier diffusion in diamond, an ultrawide-bandgap material, and demonstrated micrometer-scale periods with ~ 25 ps time resolution [5]. At facility-scale sources, TG experiments have been extended to the extreme ultraviolet (EUV) and X-ray range, reaching periods on tens of nanometer length scales [25–27].

In this work, we introduce a new, tabletop DUV TG technique to bridge the gap between micrometer-scale visible approaches and deep-nanoscale facility-scale experiments. The intermediate 197-nm, 6.3-eV DUV photon energy and subpicosecond pulse duration enable the investigation of carrier dynamics at length scales ranging from micrometers to below 300 nm in ultrawide-bandgap materials, a record for a tabletop setup. The ability to perform these experiments on a tabletop will allow for the investigation of a wider variety of materials at more length scales than have been studied previously in other TG experiments. To demonstrate and validate this new capability, we characterize surface acoustic waves (SAWs) in gold thin films and extract, with remarkable precision,

the material properties of both the film and the substrate, that agree with reference values. We then probe nanoscale electron transport in diamond and investigate the carrier density dependence of the diffusive process. The flexibility and accessibility of the DUV TG experiment enable tabletop, noncontact measurements of electron transport, phonon transport, and mechanical properties in nanoscale ultrawide-bandgap systems previously only accessible via complex sample preparation or at large facilities.

II. EXPERIMENTAL SETUP

The DUV light used in the TG experiment is the fourth harmonic of a 50-fs, 1-kHz Ti:sapphire laser amplifier system (see Supplemental Material Fig. 1 [28]). Upconversion of the ~ 800 nm fundamental wavelength occurs via second harmonic and sum frequency generation in three beta barium borate (BBO) crystals. When generating the third harmonic ($\omega + 2\omega \rightarrow 3\omega$), it is possible to achieve type I phase matching and temporal overlap in a collinear geometry, whereas the fourth harmonic generation ($\omega + 3\omega \rightarrow 4\omega$) requires the noncollinear geometry detailed in Supplemental Material section I and Refs. [28–30]. Due to phase matching conditions, it is not possible to generate DUV light below 205 nm by direct frequency doubling the second harmonic [31], which is why sum frequency generation is necessary for fourth harmonic generation of <200 nm light. The efficiency of the full up-conversion

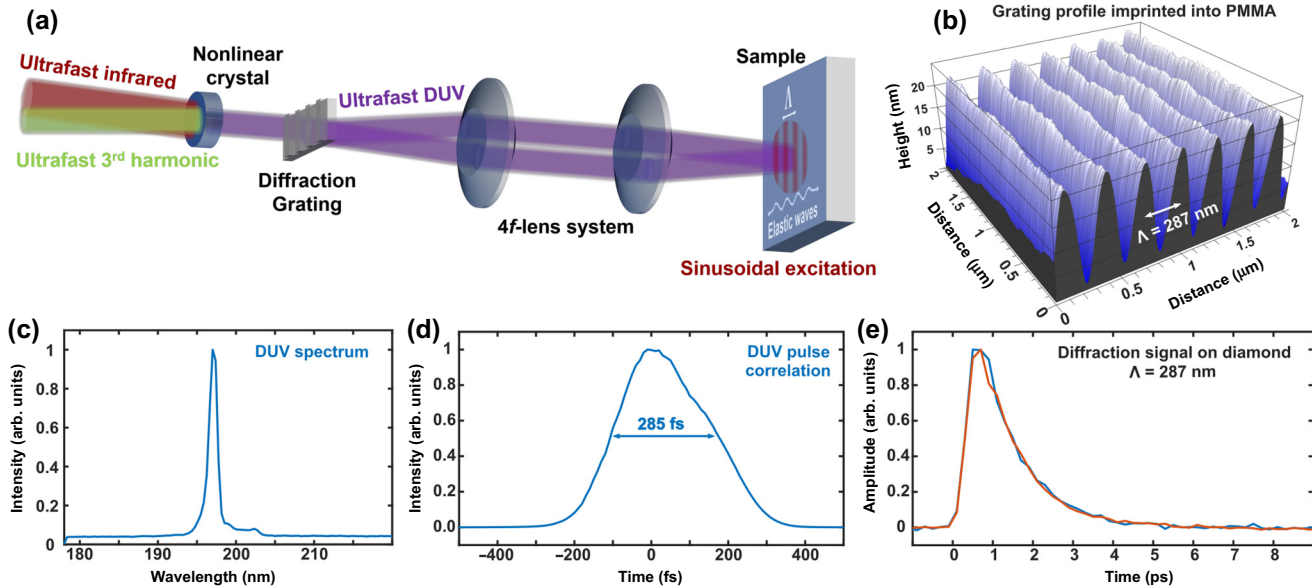


FIG. 1. DUV TG experiment. (a) The DUV light is the fourth harmonic of an ~ 800 -nm, 50-fs, 1-kHz Ti:sapphire amplifier (note that the second and third harmonic generation steps are not shown). A diffractive optic creates two DUV beams, which are focused and interfered on the sample surface using a $4f$ imaging system to generate a microscopic sinusoidal excitation profile. (b) Atomic force microscopy measurement of a 287-nm DUV interference pattern imprinted in a PMMA film. (c) DUV spectrum centered at 197-nm wavelength. (d) Correlation of the DUV (4ω) and fundamental (ω) pulses obtained by observing the intensity of third harmonic (3ω) produced by difference frequency generation in an additional BBO crystal as a function of temporal delay. (e) Time-delayed probe diffraction signal from a TG of 287-nm period on a single-crystal diamond substrate.

process is slightly less than 1%, or roughly 20% at each of the three BBO crystals. The resulting DUV light has a pulse duration below 285 fs and a spectrum centered at 197 nm, as shown in Figs. 1(c) and 1(d). We estimate the pulse duration using a difference frequency generation process, $4\omega - \omega \rightarrow 3\omega$ in an additional BBO crystal. The intensity in Fig. 1(d) is that of the generated third harmonic as a function of the temporal delay between the DUV and fundamental inputs. The full width at half maximum of a Gaussian fit to this correlation profile is 285 fs, roughly corresponding to the convolution of the DUV pulse with the ~ 50 fs fundamental pulse duration. This measurement lacks the frequency resolution necessary for a more precise characterization [32] and also does not account for dispersion in the diffraction grating and lenses used to produce the TG excitation. We observe an increase of approximately 50 fs in the full width at half maximum fit after the DUV passes through a fused silica lens, suggesting that the DUV pulse duration is moderately, but not dramatically longer after the refractive optics.

To generate a TG pattern on the sample, we split the DUV pulse train using a transmissive diffraction grating, or phase mask, optimized for diffraction efficiency into the ± 1 orders. The diffracted orders pass through the $4f$ imaging system shown in Fig. 1(a), and interfere on the sample surface to produce a TG of period

$$\Lambda = \frac{\lambda}{2 \sin(\theta/2)} = M \frac{\Lambda_0}{2}, \quad (1)$$

where $\lambda = 197$ nm is the excitation wavelength, θ is the interference angle, $\Lambda_0 = 2$ μm is the diffraction grating period and M is the imaging system magnification [33]. By changing the magnification and rotating the diffraction grating, it is possible to continuously tune the TG period from below 300 nm to several micrometers [34]. Changing the magnification also changes the beam size and consequently excitation fluence (see Sec. IV). Figure 1(b) shows an atomic force microscopy measurement of a 287 nm TG period etched into a polymethyl methacrylate (PMMA) film, after a 30-second exposure. It is also straightforward to generate TG periods down to 230 nm, using 197-nm DUV light and the numerical aperture provided by standard two-inch lenses.

We measure the relaxation of the TG in metals and wide-bandgap materials using time-delayed probe pulses derived from the same Ti:sapphire amplifier as the DUV pump. A small portion of the incident probe light diffracts from sinusoidal modulations in the refractive index, absorption, and surface height of the sample due to the electronic, thermal, and acoustic dynamics launched by the DUV TG excitation. The diffraction signal vanishes when the sample returns to equilibrium. To isolate the signal from scattered background light, we reduce the DUV pump repetition rate to 500 Hz using an optical chopper,

while probing at 1 kHz. The diffracted probe signal, at 500 Hz, is captured on a New Focus 2107 photodetector and filtered using a lock-in amplifier referenced to the pump frequency. Figure 1(e) shows the diffracted probe intensity as a function of delay time for a 287-nm TG period on a diamond substrate. The diffraction signal can be measured in reflection or transmission, with a probe wavelength of the fundamental 800 nm or a frequency-doubled 400 nm, depending on the TG period and the sample optical properties. In transmission measurements, probing at the Bragg angle, $\sin \theta_B = \lambda_p / 2\Lambda$, where λ_p is the probe wavelength and Λ is the TG period, results in constructive contributions to the diffracted probe signal across the sample depth, isolating the effects of in-plane dynamics while maintaining the maximum possible signal intensity (see Supplemental Material section III [28]). For TG periods measured in transmission, we adjust the probe incidence angle to maintain Bragg matching. As the probe is incident at the Bragg angle but is not introduced through the same $4f$ imaging system as the pump, the tilt of the probe wavefront with respect to the sample reduces the time resolution further than the approximately 285-fs correlation shown in Fig. 1(d). However, this temporal broadening effect is still estimated to be subpicosecond even for the smallest grating periods, i.e., highest probing angles, in the present study.

The diffracted signal, of intensity $I_p(t)$, may interfere with static reference probe light, of intensity I_r and relative phase ϕ , to produce a signal,

$$I(t) = I_r + I_p(t) + 2\sqrt{I_r I_p(t)} \cos \phi, \quad (2)$$

which includes a “heterodyned” term proportional to $\sqrt{I_p(t)}$ and therefore linear in the electric field of the diffracted signal. Here, we do not have a separate reference beam, but instead observe parasitic heterodyning due to interference between probe light scattered by the sample surface roughness and the diffracted signal. Heterodyning can be advantageous because tuning $I_r \gg I_p(t)$ enhances and isolates the heterodyned term, while control over ϕ allows for the isolation of various components of the material response [33]. Traditional heterodyning approaches, which generate a reference beam using the same diffraction grating and $4f$ imaging system as the pump [35], are infeasible in the present experiment due to chromatic aberrations in the lenses at DUV wavelengths. Probe light inadvertently scattered from the sample surface can also interfere with the diffracted signal at the detector, in a process known as parasitic heterodyning [11]. By periodically modulating ϕ through slight translations of the sample or diffraction grating, it is possible to estimate the degree of parasitic heterodyning. This can be substantial in the present measurements of diamond due to scatter from the ~ 0.5 -nm Ra surface roughness. In parasitic heterodyning, I_r can no longer be tuned to be much larger than

I_p , necessitating a careful treatment of the experimental signal, as discussed in Sec. IV.

Interactions between short-wavelength light and atmospheric hydrocarbons can cause the gradual deposition of a thin layer of carbon contamination on nearby surfaces [36,37]. Carbon deposition on the sample surface can alter the TG signal on a minutes-long time scale. Due to its dependence on multiphoton processes, the carbon deposition rate increases nonlinearly with laser fluence, and is negligible at sufficiently low pump and probe intensities [38]. The threshold at which carbon deposition significantly modifies DUV TG measurements of diamond is $\sim 5 \text{ mJ/cm}^2$ for the 400 nm probe light. The diamond data presented in Sec. IV is taken at a much lower probe fluence to avoid this effect. We observe no evidence of carbon deposition for the 800-nm probe light used to measure the gold films, due to its lower photon energy. We also observe no significant carbon deposition on the sample from the 200-nm pump beam in either case, likely because the pump fluence is below 1 mJ/cm^2 .

III. ACOUSTIC WAVES IN THIN GOLD FILMS

As an initial demonstration and validation of the new DUV TG experiment, we excite and measure the propagation of acoustic waves in thin gold films. This permits

the noncontact measurement of film thickness and elastic properties, which agree well with reference values. The gold films, from Angstrom Engineering[®], are nominally 50 nm thick, with a $\sim 5\text{-nm}$ chromium adhesion layer on $\langle 100 \rangle$ silicon substrates. After excitation by a DUV pump pulse, the initial sinusoidal distribution of hot electrons in the gold layer rapidly couples to the phonon system, impulsively exciting coherent longitudinal acoustic waves (LAWs) and SAWs resonant with the system geometry. The LAW propagates vertically in the gold film at the longitudinal speed of sound, dissipating upon each reflection with the substrate interface. It appears as a weak and highly damped oscillation in the experimental data at early timescales ($< 100 \text{ ps}$), as shown in Fig. 5 of the Supplemental Material. We extract the LAW frequency using a matrix pencil method (MPM) algorithm, which outperforms a fast Fourier transform in the extraction of damped frequencies with few oscillation periods [39]. The LAW frequency corresponds to a gold film thickness of $54 \pm 4 \text{ nm}$, in good agreement with the nominal value.

The SAW propagates along the sample surface in both the film and substrate, and appears as a strong oscillation in the experimental data, as shown in Fig. 2(a). The SAW wavelength λ_{SAW} is equal to the TG period, with penetration depth $\delta \sim \lambda_{\text{SAW}}/\pi$. Because the SAW penetration depth is proportional to wavelength, short (long)

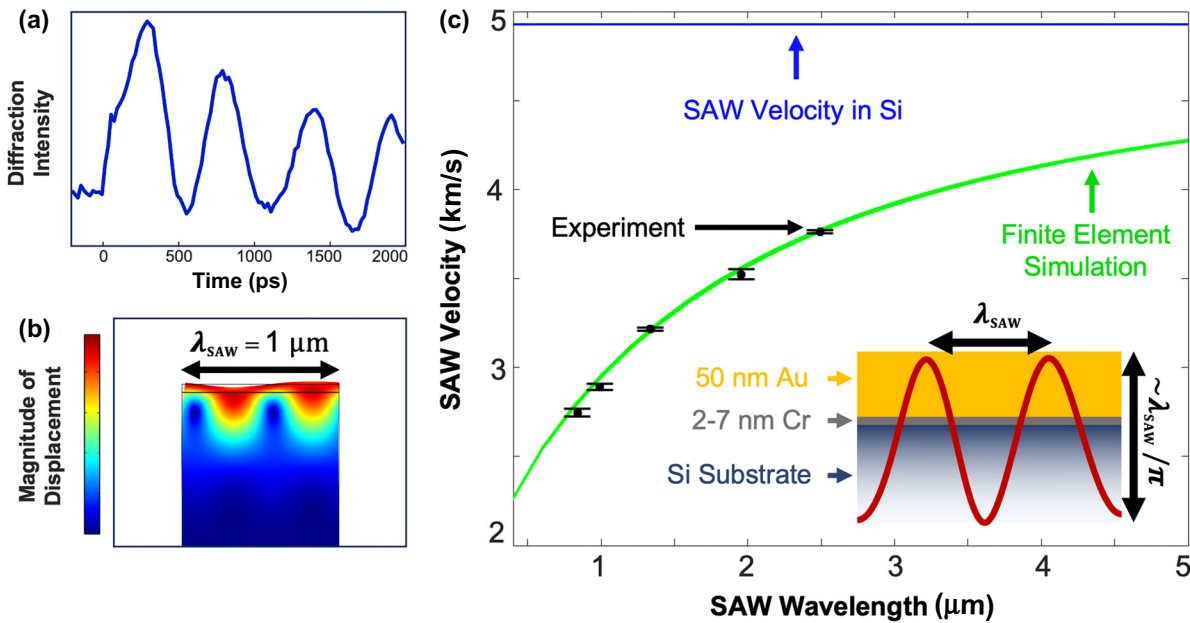


FIG. 2. TG measurements of SAWs in thin gold films (a) Experimental data displaying damped SAW oscillations in a 50-nm gold film with chromium adhesion layer on a silicon substrate, at a TG period of $1.3 \mu\text{m}$. (b) Finite element eigenfrequency calculation showing the displacement of the surface-confined SAW mode. (c) SAW dispersion (wavelength versus velocity). The experimental data (black points) are obtained by measuring the SAW frequency at various TG periods. A finite-element model with nominal material and geometric properties reproduces the experimental data (green line). The inset shows a cartoon of the SAW and sample geometry. The SAW velocity decreases at shorter wavelengths because it is increasingly confined to the softer gold film, relative to the stiffer silicon substrate (blue line).

wavelength SAWs corresponding to small (large) TG periods are more sensitive to the film (substrate) properties, respectively. Figure 2(c) shows the dispersion of the SAW velocity as a function of SAW wavelength for the film system. Shorter wavelength SAWs exhibit a reduced velocity due to increased confinement in the relatively soft gold film, as compared with the stiffer silicon substrate (blue line). The SAW wavelength for each black experimental data point was verified with an optical microscope by measuring the period of a TG pattern etched into a PMMA film. The error bars consist of uncertainty in these optical microscope measurements, along with error in the SAW frequencies extracted using the MPM algorithm described previously. The SAW dispersion in Fig. 2(c) agrees well with the results of a finite-element model based on the verified 50-nm film thickness and nominal material properties of the gold film, silicon substrate with slight strain, and chromium adhesion layer (green curve). The finite-element model performs an eigenfrequency calculation for the first few resonant modes of the sample geometry; Fig. 2(b) illustrates the displacement profile associated with the particular eigenmode identified as the SAW (details are given in Supplemental Material section II [28]). Because it can excite high-frequency SAWs in transparent materials, the present DUV TG experiment provides a noncontact means for measuring elastic properties in situations that previously required the fabrication of absorptive transducers.

IV. CARRIER DIFFUSION IN DIAMOND

Diamond is an attractive wide-bandgap semiconductor due to its high electron mobility, high electric field breakdown strength, and superior thermal conductivity [23,40]. However, fabrication issues remain a challenge in integrating it into device-level nanoelectronic architectures [41]. In addition, due to the difficulty of studying diamond with visible metrology techniques, little is known about its transport properties in device-relevant nanoscale geometries, whose dimensions are below the mean free paths of heat-carrying phonons [42]. Ultraviolet TG measurements have been used previously as a noncontact means to observe both carrier and thermal diffusion in diamond at $\sim 2\text{--}100 \mu\text{m}$ length scales [5,43–45]. However, diamond's fast transport dynamics at submicrometer length scales was not accessible due to longer laser pulse durations. At the nanoscale, investigation of electron and phonon dynamics was only achieved via transducer nanofabrication [46] or through free electron laser (FEL) TG implementations [27]. In this section, we leverage the advantages of the DUV TG technique to investigate carrier transport in single-crystal diamond on short timescales. The chemical vapor deposition (CVD) diamond sample is purchased from Applied Diamond and has $\sim 500\text{-}\mu\text{m}$ thickness, $<1 \text{ ppm}$ nitrogen impurities, and is double-side polished to $\sim 0.5\text{-nm}$ Ra surface roughness

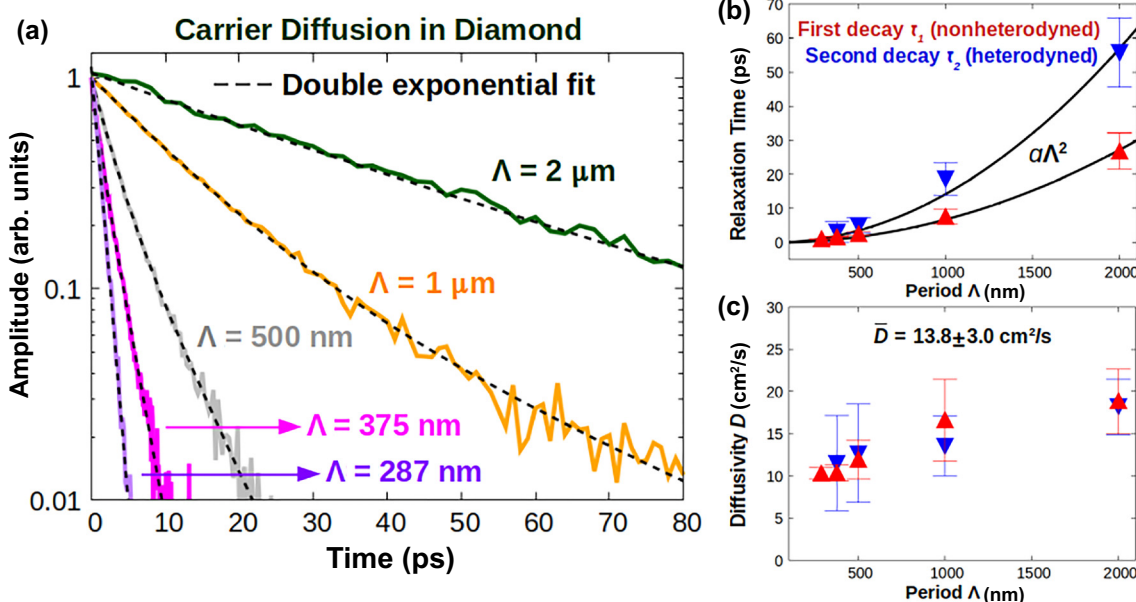


FIG. 3. Nanoscale carrier diffusion in single-crystal diamond. (a) Measured decays due to in-plane carrier diffusion at various TG periodicities. The decays have a double-exponential form because probe light scattered from the sample interferes with the diffracted signal to introduce a heterodyned term. (b) Fitted time constants for the non-heterodyned (red) and heterodyned (blue) components of the decays. As expected for carrier diffusion, the time constant scales with the square of the TG periodicity and is twice as large for the linear heterodyned term. (c) Fitted ambipolar diffusion coefficients as a function of TG periodicity. The diffusion coefficient increases slightly with TG periodicity because the magnification of the pump laser spot size on the sample results in a lower excited carrier concentration.

to enable measurements in the transmission configuration discussed in Sec. II. Prior to measurement, X-ray reflectivity confirmed minimal surface contamination.

The achievable TG periodicity in the current experiment extends down to 287 nm, limited only by the 400-nm probe wavelength, as shown in Fig. 3(a). To model the probe signal evolution, we assume that the nonequilibrium electron and hole distributions excited by the DUV pump thermalize locally on a <500 fs timescale [47,48], shorter than the measured relaxation of the TG profiles considered here. The local excited carrier density induces a proportional change in refractive index, Δn , which serves as an initial condition for the subsequent electron and hole evolution,

$$\Delta n(x, z, t = 0) = \Delta n_0[1 + \cos(qx)]e^{-\beta z}, \quad (3)$$

where x and z are coordinates in the in-plane and cross-plane directions respectively, $1/\beta$ is the pump penetration depth, and $q = 2\pi/\Lambda$ is the TG wavevector magnitude. After the excitation, the diffracted signal decays due to homogenization of the carrier density within the sample via diffusive electron and hole transport. For the small TG periods we consider, this process takes place on a picoseconds timescale as can be seen in Fig. 3(a). Therefore, density changes due to electron-hole recombination events, which occur at much longer timescales, are negligible in the present experiments. The penetration depth of 197-nm light in diamond is approximately 500 nm [49], comparable to Λ , such that carrier transport takes place in both the in-plane and cross-plane dimensions simultaneously on similar timescales. While analytical solutions of the 2D diffusion equation are available for the initial condition in Eq. (3), a probe beam incident on the TG excitation at the Bragg angle results in a diffracted signal sensitive only to the in-plane dynamics. This enables characterizing the ambipolar diffusion coefficient D from the decay of the diffracted probe intensity $I_p(t)$ considering only the in-plane component of the diffusion equation (see details in Supplemental Material section III [28]),

$$I_p(t) \sim e^{-2Dq^2t}. \quad (4)$$

However, the measured TG decays shown in Fig. 3(a) exhibit a double-exponential form, with characteristic decay times τ_1 and τ_2 . As shown in Fig. 3(b), both time constants scale as $\tau \sim q^{-2} \sim \Lambda^2$, as expected from the in-plane diffusive process outlined in Eq. (4). Because τ_2 is observed to be approximately twice τ_1 across all TG periodicities, we attribute the two exponential decays to the second and third (heterodyned) terms in Eq. (2) [35,43]. Comparison with Eq. (4) allows the identification $\tau_2 = 2\tau_1 = 1/(Dq^2)$. The resulting diffusivity fit is $D = 13.8 \pm 3.0 \text{ cm}^2/\text{s}$ for the full dataset presented in Fig. 3. The attribution of the second decay with time constant τ_2 to parasitic heterodyning is further supported by

the observation that the fitted amplitude A_2 of the second exponential decay decreases with decreasing TG periodicity because at larger diffraction angles there is less static background scatter from the sample surface (see details in Supplemental Material section III [28]).

Thus, diffusion alone explains the evolution of the carrier distribution after optical excitation, which enables the experimental characterization of the ambipolar diffusion coefficient. In turn, this indicates that ballistic electron transport effects do not manifest for the range of TG periods studied here. Nevertheless, as shown in Fig. 3(c), the diffusion coefficient increases slightly with TG periodicity when fitted separately for each value of Λ . This occurs because the magnification system described in Sec. II results in an increasing pump beam spot size, and therefore decreasing excited carrier concentration N as Λ increases. Indeed, the diffusion coefficient in diamond and other semiconductors is known to decrease with increasing carrier density [4,5,50,51]. This is generally attributed to a combination of carrier-carrier scattering [45,52] and many-body effects, which create a gradient in the bandgap along the spatial variation of N in opposition to the carrier diffusion [53]. In the present experiments, we estimate an excited carrier density in the range $2 \times 10^{17} < N < 3 \times 10^{19}/\text{cm}^3$ depending on Λ (see Supplemental Material section III [28]). Our measurements resemble previous DUV TG experiments on diamond at larger periodicities but similar carrier concentrations [5,45], as shown in Fig. 4. A recent FEL implementation of a 277-nm TG period on diamond generated

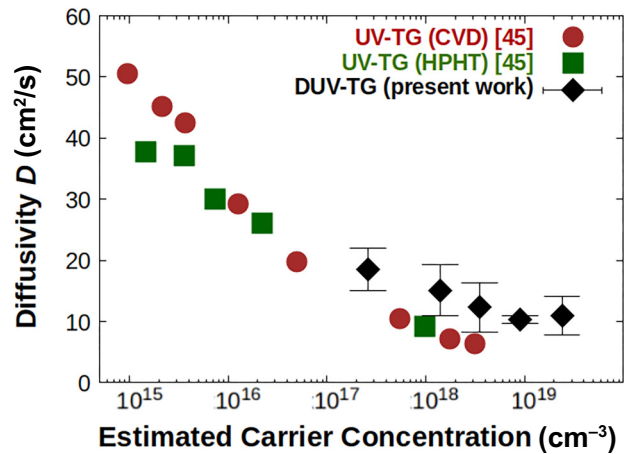


FIG. 4. Measured ambipolar diffusivity as a function of the estimated carrier density. The decrease in diffusivity is attributed to an increase in the excited carrier density as Λ decreases due to the optical magnification system. The diffusivity characterized in the present experiments roughly agrees with previous UV TG measurements of CVD and high-pressure, high-temperature (HPHT) diamond samples considering much larger TG periods, but similar carrier concentrations [45].

with 98-eV light also observed a similar carrier diffusion timescale as in the present experiment [27]. In contrast, time-of-flight experiments at much lower carrier concentrations, $N \sim 10^{13}/\text{cm}^3$, measure $D > 50 \text{ cm}^2/\text{s}$ [40,54]. We note, however, that the diffusion coefficients from different experiments are not expected to be fully compatible given the influence of defects and sample quality on carrier mobility.

V. CONCLUSION

We have demonstrated a tabletop TG metrology technique using DUV light that provides a combination of desirable capabilities for the investigation of subpicosecond, nanoscale carrier transport dynamics in semiconductors. The use of high photon energy enables the excitation of ultrawide-bandgap materials such as diamond, of interest for next-generation nanoelectronics. Moreover, the short-wavelength light allows access to the transport mechanisms under TG excitations with periods down to 287 nm, the smallest periodicity achieved so far by tabletop capabilities. Finally, the few-hundred-femtosecond pulse duration provides subpicosecond time resolution. We first validated the technique using acoustic wave propagation experiments in thin gold films, and then, we used it to measure the ambipolar diffusion coefficient for different carrier concentrations in a diamond substrate.

ACKNOWLEDGMENTS

The authors acknowledge support from the STROBE National Science Foundation Science and Technology Center, Grant No. DMR-1548924. They also acknowledge support from 3M for the development of this unique DUV apparatus. The authors thank Alex Maznev for stimulating discussions. Henry Kapteyn is partially employed by KM Labs, the company which manufactured the Ti:sapphire amplifier used in this work.

- [1] H. Eichler, G. Salje, and H. Stahl, Thermal diffusion measurements using spatially periodic temperature distributions induced by laser light, *J. Appl. Phys.* **44**, 5383 (1973).
- [2] J. A. Johnson, A. A. Maznev, J. Cuffe, J. K. Eliason, A. J. Minnich, T. Kehoe, C. M. S. Torres, G. Chen, and K. A. Nelson, Direct measurement of room-temperature nondiffusive thermal transport over micron distances in a silicon membrane, *Phys. Rev. Lett.* **110**, 025901 (2013).
- [3] V. V. Gorbachev, V. M. Durasov, R. B. Zezin, E. V. Ivakin, A. S. Rubanov, and N. A. Tatyana, Light-induced thermal gratings in natural diamond, *Phys. Status Solidi (b)* **150**, 901 (1988).
- [4] H. J. Eichler, F. Massmann, E. Biselli, K. Richter, M. Glotz, L. Konetzke, and X. Yang, Laser-induced free-carrier and temperature gratings in silicon, *Phys. Rev. B* **36**, 3247 (1987).

- [5] T. Malinauskas, K. Jarašiūnas, E. Ivakin, N. Tranchant, and M. Nesladek, Determination of carrier diffusion coefficient and lifetime in single crystalline CVD diamonds by light-induced transient grating technique, *Phys. Status Solidi A* **207**, 2058 (2010).
- [6] C. P. Weber, N. Gedik, J. E. Moore, J. Orenstein, J. Stephens, and D. D. Awschalom, Observation of spin Coulomb drag in a two-dimensional electron gas, *Nature* **437**, 1330 (2005).
- [7] J. A. Rogers and K. A. Nelson, Dis-bond detection and the possibility of interfacial stiffness measurement with real-time impulsive stimulated thermal scattering, *J. Adhes.* **50**, 1 (1995).
- [8] J. Rogers and K. Nelson, Photoacoustic determination of the residual stress and transverse isotropic elastic moduli in thin films of the polyimide PMDA/ODA, *IEEE Trans. Ultrason. Ferroelectr. Freq. Control* **42**, 555 (1995).
- [9] T. D. Frazer, Y. Zhu, Z. Cai, D. A. Walko, C. Adamo, D. G. Schlom, E. E. Fullerton, P. G. Evans, S. O. Hruszkewycz, Y. Cao, and H. Wen, Optical transient grating pumped X-ray diffraction microscopy for studying mesoscale structural dynamics, *Sci. Rep.* **11**, 19322 (2021).
- [10] T. F. Crimmins, A. A. Maznev, and K. A. Nelson, Transient grating measurements of picosecond acoustic pulses in metal films, *Appl. Phys. Lett.* **74**, 1344 (1999).
- [11] J. A. Rogers, A. A. Maznev, M. J. Banet, and K. A. Nelson, Optical generation and characterization of acoustic waves in thin films: fundamentals and applications, *Annu. Rev. Mater. Sci.* **30**, 117 (2000).
- [12] S. Huberman, R. A. Duncan, K. Chen, B. Song, V. Chiloyan, Z. Ding, A. A. Maznev, G. Chen, and K. A. Nelson, Observation of second sound in graphite at temperatures above 100 k, *Science* **364**, 375 (2019).
- [13] J. Janušonis, T. Jansma, C. L. Chang, Q. Liu, A. Gatilova, A. M. Lomonosov, V. Shalagatskyi, T. Pezeril, V. V. Temnov, and R. I. Tobey, Transient grating spectroscopy in magnetic thin films: simultaneous detection of elastic and magnetic dynamics, *Sci. Rep.* **6**, 29143 (2016).
- [14] F. Hofmann, M. P. Short, and C. A. Dennett, Transient grating spectroscopy: an ultrarapid, nondestructive materials evaluation technique, *MRS Bull.* **44**, 392 (2019).
- [15] Y. Yan, L. Cheng, and K. A. Nelson, The temperature-dependent distribution of relaxation times in glycerol: time-domain light scattering study of acoustic and mountain-mode behavior in the 20 MHz–3 GHz frequency range, *J. Chem. Phys.* **88**, 6477 (1988).
- [16] C. Frez, G. J. Diebold, C. D. Tran, and S. Yu, Determination of thermal diffusivities, thermal conductivities, and sound speeds of room-temperature ionic liquids by the transient grating technique, *J. Chem. Eng. Data* **51**, 1250 (2006).
- [17] A. Ehn, J. Zhu, X. Li, and J. Kiefer, Advanced laser-based techniques for gas-phase diagnostics in combustion and aerospace engineering, *Appl. Spectrosc.* **71**, 341 (2017).
- [18] H. Eichler, P. Guünter, and D. Pohl, *Laser Induced Dynamic Gratings* (Springer-Verlag Berlin Heidelberg, Heidelberg, 1986).
- [19] U. Choudhry, T. Kim, M. Adams, J. Ranasinghe, R. Yang, and B. Liao, Characterizing microscale energy transport in materials with transient grating spectroscopy, *J. Appl. Phys.* **130**, 231101 (2021).

- [20] A. B. Robbins, S. X. Drakopoulos, I. Martin-Fabiani, S. Ronca, and A. J. Minnich, Ballistic thermal phonons traversing nanocrystalline domains in oriented polyethylene, *Proc. Natl. Acad. Sci.* **116**, 17163 (2019).
- [21] T. Kim, D. Ding, J.-H. Yim, Y.-D. Jho, and A. J. Minnich, Elastic and thermal properties of free-standing molybdenum disulfide membranes measured using ultrafast transient grating spectroscopy, *APL Mater.* **5**, 086105 (2017).
- [22] J. Y. Tsao, *et al.*, Ultrawide-bandgap semiconductors: research opportunities and challenges, *Adv. Electron. Mater.* **4**, 1600501 (2018).
- [23] R. J. Warzoha, A. A. Wilson, B. F. Donovan, N. Donmezzer, A. Giri, P. E. Hopkins, S. Choi, D. Pahinkar, J. Shi, S. Graham, Z. Tian, and L. Ruppalt, Applications and impacts of nanoscale thermal transport in electronics packaging, *J. Electron. Packag.* **143**, 020804 (2021).
- [24] C. Yuan, R. Hanus, and S. Graham, A review of thermoreflectance techniques for characterizing wide bandgap semiconductors' thermal properties and devices' temperatures, *J. Appl. Phys.* **132**, 220701 (2022).
- [25] F. Bencivenga, *et al.*, Nanoscale transient gratings excited and probed by extreme ultraviolet femtosecond pulses, *Sci. Adv.* **5**, eaaw5805 (2019).
- [26] F. Steinbach, U. Atxitia, K. Yao, M. Borchert, D. Engel, F. Bencivenga, L. Foglia, R. Mincigrucci, E. Pedersoli, D. De Angelis, M. Pancaldi, D. Fainozzi, J. S. Pelli Cresi, E. Paltanin, F. Capotondi, C. Masciovecchio, S. Eisebitt, and C. von Korff Schmising, Exploring the fundamental spatial limits of magnetic all-optical switching, *Nano Lett.* **24**, 6865 (2024).
- [27] A. A. Maznev, *et al.*, Generation of coherent phonons by coherent extreme ultraviolet radiation in a transient grating experiment, *Appl. Phys. Lett.* **113**, 221905 (2018).
- [28] See Supplemental Material at <http://link.aps.org-supplemental/10.1103/PhysRevApplied.22.054007> for more information on the experimental setup, the gold acoustics analysis, and the carrier diffusion in diamond analysis. The Supplemental Material also includes Refs. [55–63].
- [29] J. Ringling, O. Kittelmann, F. Noack, G. Korn, and J. Squier, Tunable femtosecond pulses in the near vacuum ultraviolet generated by frequency conversion of amplified Ti:sapphire laser pulses, *Opt. Lett.* **18**, 2035 (1993).
- [30] F. Rotermund and V. Petrov, Generation of the fourth harmonic of a femtosecond Ti:sapphire laser, *Opt. Lett.* **23**, 1040 (1998).
- [31] B. E. Schmidt, P. Lassonde, G. Ernotte, M. Clerici, R. Morandotti, H. Ibrahim, and F. Légaré, in *2017 Conference on Lasers and Electro-Optics (CLEO)* (IEEE, San Jose, CA, USA, 2017), p. 1.
- [32] C. G. Durfee, S. Backus, H. C. Kapteyn, and M. M. Murnane, Intense 8-fs pulse generation in the deep ultraviolet, *Opt. Lett.* **24**, 697 (1999).
- [33] A. A. Maznev, K. A. Nelson, and J. A. Rogers, Optical heterodyne detection of laser-induced gratings, *Opt. Lett.* **23**, 1319 (1998).
- [34] A. Vega-Flick, J. K. Eliason, A. A. Maznev, A. Khanolkar, M. Abi Ghanem, N. Boechler, J. J. Alvarado-Gil, and K. A. Nelson, Laser-induced transient grating setup with continuously tunable period, *Rev. Sci. Instrum.* **86**, 123101 (2015).
- [35] J. A. Johnson, A. A. Maznev, M. T. Bulsara, E. A. Fitzgerald, T. C. Harman, S. Calawa, C. J. Vineis, G. Turner, and K. A. Nelson, Phase-controlled, heterodyne laser-induced transient grating measurements of thermal transport properties in opaque material, *J. Appl. Phys.* **111**, 023503 (2012).
- [36] R. R. Kunz, V. Liberman, and D. K. Downs, Experimentation and modeling of organic photocontamination on lithographic optics, *J. Vac. Sci. Technol. B* **18**, 1306 (2000).
- [37] J. Hollenshead and L. Klebanoff, Modeling radiation-induced carbon contamination of extreme ultraviolet optics, *J. Vac. Sci. Technol. B* **24**, 64 (2006).
- [38] Z. Hubka, J. Novák, I. Majerová, J. T. Green, P. K. Velpula, R. Boge, R. Antipenkov, V. Šobr, D. Kramer, K. Majer, J. A. Naylor, P. Bakule, and B. Rus, Mitigation of laser-induced contamination in vacuum in high-repetition-rate high-peak-power laser systems, *Appl. Opt.* **60**, 533 (2021).
- [39] A. Beardo, J. L. Knobloch, L. Sendra, J. Bafaluy, T. D. Frazer, W. Chao, J. N. Hernandez-Charpak, H. C. Kapteyn, B. Abad, M. M. Murnane, F. X. Alvarez, and J. Camacho, A general and predictive understanding of thermal transport from 1D- and 2D-confined nanostructures: theory and experiment, *ACS Nano* **15**, 13019 (2021).
- [40] J. Isberg, J. Hammersberg, E. Johansson, T. Wikström, D. J. Twitchen, A. J. Whitehead, S. E. Coe, and G. A. Scarsbrook, High carrier mobility in single-crystal plasma-deposited diamond, *Science* **297**, 1670 (2002).
- [41] D. Araujo, M. Suzuki, F. Lloret, G. Alba, and P. Villar, Diamond for electronics: materials, processing and devices, *Materials* **14**, 7081 (2021).
- [42] W. Li, N. Mingo, L. Lindsay, D. A. Broido, D. A. Stewart, and N. A. Katcho, Thermal conductivity of diamond nanowires from first principles, *Phys. Rev. B* **85**, 195436 (2012).
- [43] E. V. Ivakin, A. V. Sukhodolov, V. G. Ralchenko, A. V. Vlasov, and A. V. Khomich, Measurement of thermal conductivity of polycrystalline CVD diamond by laser-induced transient grating technique, *Quantum Electron.* **32**, 367 (2002).
- [44] M. Kozák, F. Trojánek, and P. Malý, Optical study of carrier diffusion and recombination in CVD diamond, *Phys. Status Solidi A* **210**, 2008 (2013).
- [45] P. Ščajev, T. Malinauskas, L. Lubys, E. Ivakin, M. Nesladek, K. Haenen, and K. Jarašiūnas, Optical monitoring of nonequilibrium carrier diffusion in single crystalline CVD and HPHT diamonds under high optical excitation, *Phys. Status Solidi RRL* **5**, 193 (2011).
- [46] T. D. Frazer, J. L. Knobloch, K. M. Hoogeboom-Pot, D. Nardi, W. Chao, R. W. Falcone, M. M. Murnane, H. C. Kapteyn, and J. N. Hernandez-Charpak, Engineering nanoscale thermal transport: size- and spacing-dependent cooling of nanostructures, *Phys. Rev. Appl.* **11**, 024042 (2019).
- [47] N. Tandon, J. Albrecht, and L. Ram-Mohan, Electron–phonon coupling and associated scattering rates in diamond, *Diam. Relat. Mater.* **56**, 1 (2015).
- [48] D. O. Nielsen and M. V. Fischetti, Thermalization of radiation-induced electrons in wide-bandgap materials: a

- first-principles approach, *Appl. Phys. Lett.* **123**, 252107 (2023).
- [49] A. Taylor, P. Ashcheulov, P. Hubík, Z. Weiss, L. Klimša, J. Kopeček, J. Hrabovsky, M. Veis, J. Lorinčík, I. Elantyev, and V. Mortet, Comparative determination of atomic boron and carrier concentration in highly boron doped nano-crystalline diamond, *Diam. Relat. Mater.* **135**, 109837 (2023).
- [50] M. Kozák, F. Trojánek, and P. Malý, Temperature and density dependence of exciton dynamics in IIA diamond: experimental and theoretical study, *Phys. Status Solidi A* **211**, 2244 (2014).
- [51] N. Naka, H. Morimoto, and I. Akimoto, Excitons and fundamental transport properties of diamond under photo-injection, *Phys. Status Solidi A* **213**, 2551 (2016).
- [52] C.-M. Li, T. Sjodin, and H.-L. Dai, Photoexcited carrier diffusion near a Si(111) surface: non-negligible consequence of carrier-carrier scattering, *Phys. Rev. B* **56**, 15252 (1997).
- [53] J. F. Young and H. M. van Driel, Ambipolar diffusion of high-density electrons and holes in Ge, Si, and GaAs: many-body effects, *Phys. Rev. B* **26**, 2147 (1982).
- [54] M. Nesladek, A. Bogdan, W. Deferme, N. Tranchant, and P. Bergonzo, Charge transport in high mobility single crystal diamond, *Diam. Relat. Mater.* **17**, 1235 (2008). Proceedings of Diamond 2007, the 18th European Conference on Diamond, Diamond-Like Materials, Carbon Nanotubes, Nitrides and Silicon Carbide.
- [55] B. McBennett, Non-contact measurements of nanoscale phonon and electron transport with ultrafast, coherent short-wavelength light. Ph.D. thesis, University of Colorado at Boulder, 2024.
- [56] COMSOL AB, Stockholm, Sweden, “COMSOL Multiphysics® v. 5.3a.”.
- [57] M. A. Hopcroft, W. D. Nix, and T. W. Kenny, What is the Young’s modulus of silicon?, *J. Microelectromech. Syst.* **19**, 229 (2010).
- [58] D. R. Lide, *CRC Handbook of Chemistry and Physics* (CRC Press, Boca Raton, Florida, 2005), 85 ed.
- [59] Y. Y. Kim, An advanced characterization method for the elastic modulus of nanoscale thin-films using a high-frequency micromechanical resonator, *Materials* **10**, 806 (2017).
- [60] Webelements periodic table, <https://www.webelements.com/> (accessed July 2024).
- [61] J. P. Hugonin and P. Lalanne, Reticolo software for grating analysis, [ArXiv:2101.00901](https://arxiv.org/abs/2101.00901).
- [62] P. Ščajev, V. Gudelis, K. Jarašiūnas, I. Kisialiou, E. Ivakin, M. Nesladek, and K. Haenen, Carrier recombination and diffusivity in microcrystalline CVD-grown and single-crystalline HPHT diamonds, *Physica Status Solidi (a)* **209**, 1744 (2012).
- [63] M. G. Moharam, E. B. Grann, D. A. Pommet and T. K. Gaylord, Formulation for stable and efficient implementation of the rigorous coupled-wave analysis of binary gratings, *J. Opt. Soc. Am. A* **12**, 1068 (1995).